TIA: a forward model and analyzer for Talbot interferometry experiments of dense plasmas

G. Pérez-Callejo,[1,2,a)] V. Bouffetier,[1,3] L. Ceurvorst,[1,4] T. Goudal,[1] M. P. Valdivia,[5,6] D. Stutman,[5,7] and A. Casner[1,8]

[1)] *Université de Bordeaux-CNRS-CEA, Centre Lasers Intenses et Applications (CELIA), UMR 5107, F-33405 Talence, France*

[2)] *Departamento de Física Teórica Atómica y Óptica, Universidad de Valladolid, 47011 Valladolid, Spain*

[3)] *European XFEL GmbH, Holzkoppel 4, 22869 Schenefeld, Germany*

[4)] *Laboratory for Laser Energetics, 250 East River Road, Rochester, NY 14623, United States of America*

[5)] *Department of Astrophysics and Astronomy, Johns Hopkins University, Baltimore, Maryland 21218, USA*

[6)] *Center for Energy Research, University of California San Diego, La Jolla, California 92093, USA*

[7)] *Extreme Light Infrastructure - Nuclear Physics, 077125 Bucharest-Magurele, Romania*

[8)] *CEA-CESTA, 15 avenue des Sablières, CS 60001, 33116 Le Barp CEDEX, France*

Interferometry is one of the most sensitive and successful diagnostic methods for plasmas. However, owing to the design of most common interferometric systems, the wavelengths of operation, and therefore the range of densities and temperatures that can be probed, are severely limited. Talbot-Lau Interferometry offers the possibility of extending interferometry measurements to X-ray wavelengths by means of the *Talbot effect*. While there have been several proof-of-concept experiments showing the efficacy of this method, it is only recently that experiments to probe High Energy Density (HED) plasmas using Talbot-Lau Interferometry are starting to take place. To improve these experimental designs, we present here the Talbot-Interferometry Analyzer (TIA) tool, a forward model for generating and postprocessing synthetic X-ray interferometry images from a Talbot-Lau interferometer. Although TIA can work with any two-dimensional hydrodynamic code to study plasma conditions as close to reality as possible, this software has been designed to work by default with output files from the hydrodynamic code FLASH, making the tool user-friendly and accessible to the general plasma physics community. The model has been built into a standalone app which can be installed by anyone with access to the MATLAB runtime installer and is available upon request to the authors.

I. INTRODUCTION

Diagnosing the properties of High Energy Density (HED) laboratory plasmas, such as those present in Inertial Confinement Fusion (ICF), is fundamental to understanding their evolution and interaction[1]. However, these measurements are challenging to obtain given the usually extreme temperature and density conditions involved as well as the small time and spatial scales over which some of these interactions occur. In this context, interferometry methods have become a useful tool, owing to the high spatial resolution that can be achieved with them. However, since HED plasmas are opaque to the frequencies characteristic of visible light, X-ray radiation must be used instead when studying this plasma regime[2].

For X-ray energies, conventional interferometry methods cannot be applied, as most materials are transparent and non-reflective to X-rays. However, it is still possible to generate X-ray interference patterns by using diffraction gratings and making a wave interfere with itself. Particularly useful tools in this case are the *Talbot effect*[3] and the *Lau effect*[4].

Talbot-Lau interferometry is most commonly used for clinical applications of X-ray interferometry[5,6], although recently, its use in HED experiments and high power laser facilities has seen significant growth[7–11]. This is owed to its promising capabilities to measure small-angle scattering and density gradients in the electron species[12] in addition to classical absorption radiography. However, because of the limited amount of data that can usually be obtained in these experiments, having dedicated shots to set up the interferometer is highly detrimental to the experimental success.

In this context, we present the Talbot Interferometry Analyzer (TIA) code[13], a forward model for simulating and postprocessing Talbot and Talbot-Lau interferometry images of dense plasmas. The main advantage of TIA with respect to other pre-existing tools is that, rather than simple geometrical shapes, it produces synthetic interferometry images of complex plasma systems using the output from hydrodynamic simulations. The TIA code produces realistic interferometric images given a complete set of specified instrumental parameters, thereby allowing users to reliably design their experiments be-

[a)] Electronic mail: gabriel.perez.callejo@uva.es

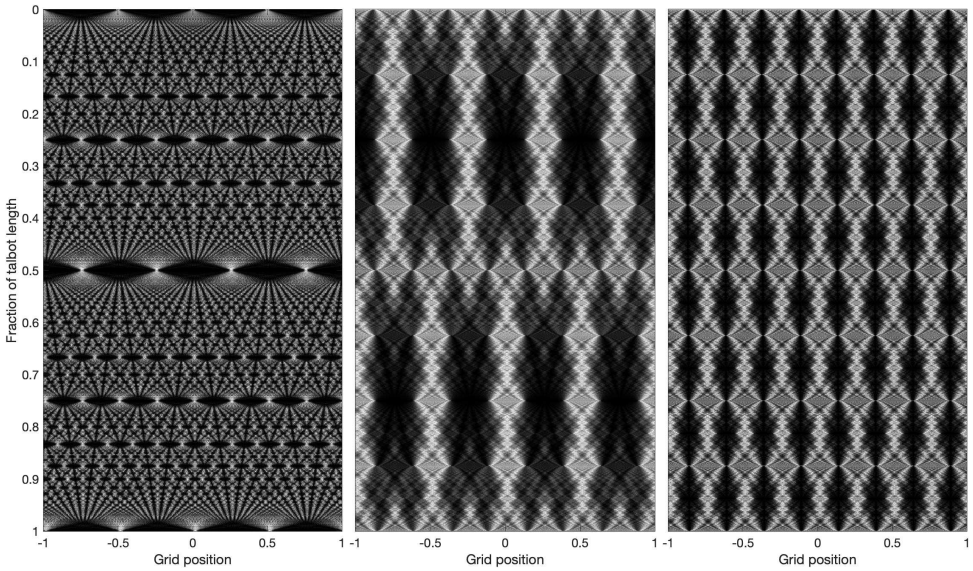

(a) (b) (c)

FIG. 1. Examples of Talbot carpets generated with TIA for: (a) a transmission grating with small apertures; (b) a $\pi/2$-shift grating with a duty cycle of 0.5 and (c) a π-shift grating with a duty cycle of 0.5.

forehand. It has been built into a standalone graphical user interface using the MATLAB App Designer tool and is available upon request to the authors.

The paper is structured as follows. In Section II a mathematical and physical description of Talbot interferometry is given. Section III details the operation of TIA and how the double diffraction problem from a two-grating interferometer is solved within the code. In Section III C we describe the postprocessing module of TIA, which can be used to determine the value of the magnitudes that can be extracted from the interferometry images. We then present the analysis of a particular example in Section IV, using a Rayleigh-Taylor instability simulation. Finally, Section V presents the conclusions of the paper and discusses future work.

II. TALBOT INTERFEROMETRY

The Talbot effect exhibits itself in the fact that when a plane wave is diffracted by a periodic grating with small apertures, an exact image of this grating is generated at a distance z_T of the original grating where z_T is called the *Talbot length*. This self-image is generated periodically at distances $n \cdot z_T$, where n is a natural number. Additionally, at $0.5z_T$, the same pattern, shifted by half a grating period, is observed; and at any rational fraction of z_T, a similar image is produced but with a smaller periodicity. This generates a fractal pattern known as a *Talbot carpet* which is shown in Figure 1a.

For a grating of period p and a wave of wavelength λ, the exact expression of the Talbot length is

$$z_T = \frac{\lambda}{1 - \sqrt{1 - \frac{\lambda^2}{p^2}}}. \tag{1}$$

In most practical uses concerning X rays, it is safe to assume that $\lambda \ll p$. In that case, by expanding Equation 1 in a power series and keeping the first term, the Talbot length can be approximated as

$$z_T = \frac{2p^2}{\lambda}. \tag{2}$$

However, this effect is slightly modified in the case of phase gratings. Most phase gratings have a duty cycle of 0.5. That is, only half of the grating is producing the phase shift, resulting in effective apertures equal to the size of their separation. Under these conditions, the assumption of small apertures does not hold any longer and the resulting Talbot carpet pattern presents a different shape, with self-recreations of the grating observed at distances

$$d_m = \frac{m}{4} \cdot \frac{2p_{\text{eff}}^2}{\lambda}, \tag{3}$$

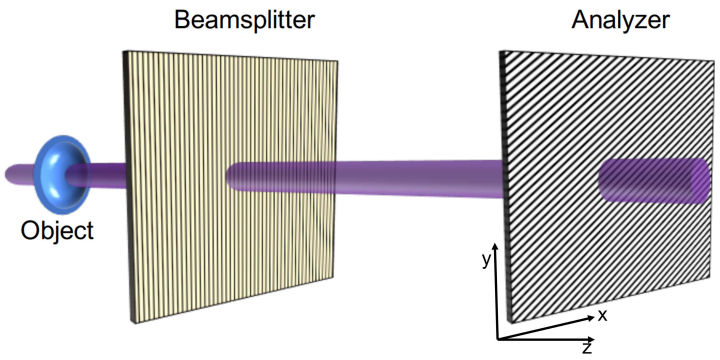

FIG. 2. Schematic of a Talbot interferometer as used in TIA. A plane wave of X-rays probes an object defined by the density and temperature profiles from the FLASH output files. The resulting wave is then diffracted by a phase grating (the *beamsplitter*), and propagates in vacuum until it reaches a transmission grating (the *analyzer*). The resulting wave is then imprinted upon a general detector. Note that the analyzer grating can be rotated by a specified angle with respect to the beamsplitter to use Moiré interferometry. A coordinate system has been added to the image for clarity.

where m is and odd integer referred to as the *Talbot order* and p_{eff} is the effective period of the grating. This effective period is related to the real period of the grating p as

$$p_{\text{eff}} = \begin{cases} p & \text{for } \pi/2\text{-shift gratings} \\ p/2 & \text{for } \pi\text{-shift gratings} \end{cases}. \tag{4}$$

This effect is shown in Figures 1b for a $\pi/2$-shift grating, and 1c for a π-shift grating. In these two images, the gratings producing the pattern have the same period. However, in the π-shift case the self-images recreate the effective periodicity rather than the true value.

A Talbot interferometer takes advantage of this phenomenon through the consecutive use of a phase grating and a transmission grating[14–18]. A coherent wave probes a plasma, and therefore, a phase-shift pattern is generated on the wavefront. This is then diffracted by a phase grating, called the *beamsplitter*, which imprints an additional periodic phase pattern on the wave, and generates a pseudo-Talbot carpet profile. The second grating, called the *analyzer*, is a transmission grating placed at a distance d_m from the beamsplitter grating (see Equation 3), where a recreation of the first grating's diffraction pattern is generated. The function of the analyzer is to convert the phase differences in the interference pattern to intensity changes, so that they can be directly observed.

A schematic of a Talbot interferometer using a coherent light source is shown in Figure 2. In this figure, it can be seen that the lines of the beamsplitter and the analyzer grating are not oriented in the same directions, but there is some angle between them. Although this is not strictly necessary for general Talbot interferometry, in many cases, a small rotation angle ($\sin(\theta) \approx \theta$) between the two gratings is introduced to generate a Moiré pattern on the observed image[8–10,14,19–28]. This introduces an additional periodicity in the direction perpendicular to the fringes, which, if the two gratings have the same effective periodicity p_{eff}, depends on the angle as

$$p_{\text{Moiré}} = \frac{p_{\text{eff}}/2}{\sin(\theta/2)} \sim \frac{p_{\text{eff}}}{\theta}. \tag{5}$$

This periodicity can be easily tuned by changing the angle between the gratings. This is particularly interesting for probing dense plasmas, which requires wavelengths of the order of 1-10 Å. In order to keep the size of the Talbot interferometer manageable, this requires the effective period of the gratings to be of the order of $< 20\,\mu$m. Although possible, using detectors that can resolve fringes with said periodicity (the detector resolution must be $< p_{\text{fringes}}/2$) is demanding. For this reason, introducing a Moiré periodicity that can be adjusted to fall within the detector resolution is extremely useful, and it enables single-shot imaging of HED plasmas instead of the phase-stepping methods commonly used in medical sciences. Note that the maximum spatial resolution that can be achieved using Moiré interferometry is on the order of $\sim 2-3$ fringe periods in the direction perpendicular to the Moiré fringes. Along the fringes' direction, the resolution is independent of the periodicity and is given by the size of the source and the pixels, among other characteristics of the system.

Although with the rise of Free Electron Lasers such as the European XFEL[29,30], SACLA[31] or LCLS[32], the use of tunable, transversely coherent X-ray radiation[33] has become possible, thus simplifying the use of X-ray interferometry for HED plasma experiments, most commonly used X-ray sources do not produce coherent ra-

diation. In these cases, an additional transmission grating can be placed between the X-ray source and the object to be probed. This generates locally coherent light that can then recreate the Talbot carpet patterns in what is known as the Lau effect[4,34]. This method, which introduces magnification in the system by using divergent sources, is referred to as Talbot-Lau interferometry.

III. TIA OPERATION

TIA can work with any two-dimensional hydrodynamic code, as it only requires density, temperature and ionization profiles to work. On its default mode, it is designed to work with the file structure of the FLASH hydrodynamic code[35–37], one of the most commonly used tools within the academic community to interpret HED experiments[38,39], which includes an extensive suite of physics capabilities and tools for HED Physics[37].

While using the code with three-dimensional simulations is possible, in its first version TIA is designed for 2D cases only. The reason for this choice is that 3D hydrodynamic simulations of plasmas are generally computationally expensive. 2D simulations are commonly used as a first approach to experimental designs, taking advantage of natural symmetries present in the system, while being computationally affordable.

The TIA code is composed of three different modules: the wavefront calculator, the diffraction solver, and the postprocessing module. The wavefront calculator converts the output from the hydrodynamic simulation to a 3D plasma object and calculates the wavefront resulting from a plane wave probing that plasma. The second module solves the diffraction and propagation of said wavefront through the two gratings that make up the Talbot interferometer and the space between them (and between the interferometer and the detector). The final module postprocesses the interferometry images to obtain transmission, dark field and phase shift images. In this section, we detail the operation of each of these modules.

A. Wavefront calculator

For interferometry analysis, a spatially coherent light source is necessary. As mentioned above, in some experiments, an X-ray Free Electron Laser (XFEL) is used, whereas in others, a coherent X-ray source is obtained by sending the incoherent radiation through a first grating prior to probing the object. This is referred to as Talbot-Lau interferometry, as mentioned in the previous section. The first grating then generates several smaller sources that are locally coherent[17].

In the case of TIA, the code starts by assuming a plane wave whose wavelength or photon energy is specified by the user. It is also possible to operate the code in Talbot-Lau mode, using a divergent source (equivalent to the additional grating required in this case). While this is not strictly Talbot-Lau interferometry, since instead of a collection of locally coherent divergent sources, TIA considers only one coherent divergent source, the physical behavior of both systems is equivalent. If this mode is selected, TIA models the system by doing a simple geometric correction to account for the magnification, as shown in Figure 3. In this case, the period of the beamsplitter and analyzer gratings are corrected as

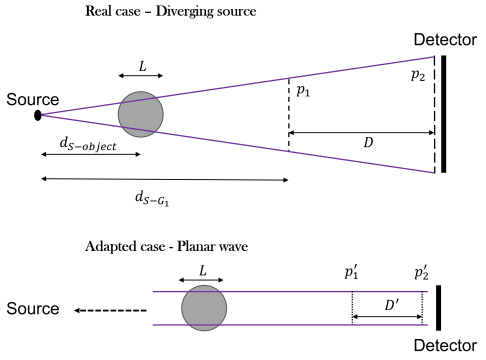

FIG. 3. Schematic of the adaptation of experimental setups with divergent sources to the plane wave approximation.

$$p_1' = p_1 \cdot \frac{d_{S-object}}{d_{S-G_1}}, \tag{6}$$

$$p_2' = p_2 \cdot \frac{d_{S-object}}{D + d_{S-G_1}}, \tag{7}$$

where $d_{S-object}$ is the distance from the source to the plasma object, d_{S-G_1} is the distance from the source to the beamsplitter grating and D is the distance between the gratings as defined in Figure 3. The distance D' can then be obtained as the equivalent Talbot order for a grating of period p_1'. Since in this case, the first grating acts like an *effective* coherent source, the distances d are measured from this grating rather than from the actual incoherent source. After applying this correction, the system is equivalent to using a collimated coherent beam.

In order to calculate the effects of the plasma object on the wavefront, TIA assumes that, although the experimental X-ray source might be divergent, it does not diverge significantly over the length scale of the object to be probed. This approximation is valid as long as the distance between the source and the beamsplitter is significantly larger than the size of the plasma object (following the notation in Figure 3, $d_{S-G_1} \gg L$). This is the case for most HED plasma applications, where the plasma is of the order of hundreds of microns, whereas the distance between source and beamsplitter is of the order of centimeters.

The plane wave generated by the code has a constant amplitude $E_0 = 1$, travels in the direction of the optical axis of the interferometer (z in Figure 2), and probes the plasma object from the hydrodynamic simulation. Since TIA works with 2D objects, to simulate the third dimension, the user can choose to either add a constant thickness to the simulation or rotate the plasma around $x = 0$ or $y = 0$ to simulate cylindrical symmetry (hydrodynamic simulations with cylindrical symmetry are in most cases designed so that the axis of the cylinder coincides with either the vertical or the horizontal axis of the images). In any case, the result is a 3D plasma object which can be probed by the wave.

After the wave has probed the plasma, its phase has been modified, yielding a wavefront exiting the plasma of the form

$$E_{Plasma}(x, y) = E_0 \cdot e^{i\Delta\tilde{\phi}(x,y)}, \tag{8}$$

where i is the imaginary unit and $\Delta\tilde{\phi}(x, y)$ is the spatially resolved change in phase introduced by the plasma. This depends on the wavenumber of the radiation, the thickness of the plasma, and its refractive index as

$$\Delta\tilde{\phi}(x, y) = \sum_z n(x, y, z) \cdot k \cdot \Delta z, \tag{9}$$

where z is the optical axis of the interferometer, $n(x, y, z)$ is the refractive index of the plasma at the corresponding X-ray energy, k is the wavenumber of the radiation, and Δz is the size of the calculation cell. Note that the real part of the refractive index will contribute to Equation 8 as a phase shift, whereas its imaginary component will result in a negative exponential corresponding to the attenuation of the electric field. Although in reality, this sum is an integral, TIA works with calculation cells of a discrete size. Depending on whether the user has specified a cylindrical symmetry or a constant thickness, the dependence on z of the refractive index may be dropped.

Calculating the refractive index of a plasma in the X-ray regime is not a trivial problem. A detailed study would require expensive calculations of the atomic structure of the elements present within the plasma for the ionization states characteristic of the corresponding temperature and density conditions, to correctly account for bound and free electrons[40]. To this end, TIA gives the user two different options.

In one case, the user can specify the complex refractive index at the wavelength of consideration as $n = 1 - \delta - i\beta$ by specifying the values of δ and β for a given mass density.

However, if the temperature dependence is important or if there are different materials with significantly different refractive indices present in the plasma, this approach might not be adequate. In this case, the user can specify that the refractive index is calculated with the Drude model, which assumes a collisional, unmagnetized plasma. In that case, at each cell TIA calculates the plasma frequency ω_P and the electron-ion collision frequency ν_{ei} (in units of s^{-1}) as[41]

$$\omega_P = \sqrt{\frac{n_e e^2}{m_e \varepsilon_0}}, \tag{10}$$

$$\nu_{ei} = \frac{\bar{Z} \cdot \ln(\Lambda)}{3.4 \times 10^5} \cdot \frac{n_e}{T_e^{3/2}}, \tag{11}$$

where n_e is the density of free electrons in the plasma in cm^{-3}, e and m_e represent the electron charge and mass respectively, ε_0 corresponds to the electric permittivity of vacuum, $\bar{Z}$ is the mean ionization state of the plasma at the point of consideration, T_e is the electron temperature in eV and $\ln(\Lambda)$ is the Coulomb logarithm, obtained as[42]

$$\begin{aligned} \ln(\Lambda) = & \\ &= 23 - \log\left(n_e^{1/2} T_e^{-3/2} \bar{Z}\right), \quad T_i \frac{m_e}{m_i} < T_e < 10\bar{Z}^2 \text{ eV} \\ &= 24 - \log\left(n_e^{1/2} T_e^{-1}\right), \qquad T_i \frac{m_e}{m_i} < 10\bar{Z}^2 \text{ eV} < T_e \end{aligned} \tag{12}$$

where m_i and T_i are the mass of the ions and the ion temperature respectively.

Once these values have been obtained for each (x, y, z) point using the spatial distribution of density, temperature and ionization obtained from the output of the hydrodynamic simulation, the refractive index is calculated as[43,44]

$$n = \sqrt{1 - \frac{\omega_p^2}{\omega^2 + \nu_{ei}^2} \cdot \left(1 - i\frac{\nu_{ei}}{\omega}\right)}, \tag{13}$$

where ω is the frequency of the X rays. Given that this model is not perfect, the user can define a different model for the refractive index within the code, if desired.

It is now possible, combining equations 8, 9 and 13, to obtain the wavefront produced after probing the plasma object as a 2D complex matrix. It is then sent through the beam-splitter grating of the interferometer, which the user can select to be either a π-phase, $\pi/2$-phase or a transmission grating. Additionally, the user can select the orientation of the grating fringes to be either vertical (as shown in the schematic presented in Figure 2) or horizontal, depending on the characteristics of the plasma object. For the second grating, the user can specify an angle of rotation θ with respect to the first one.

The effect of the gratings is introduced by the code as an additional mask that is applied to the wavefront. For a horizontal grating rotated a small angle θ, the response of the grating is characterized by two parameters η_1 and η_2 as

$$G(x, y) = \begin{cases} \eta_1, & \Xi - \lfloor \Xi \rfloor < 0.5 \\ a, & \text{otherwise} \end{cases}, \tag{14}$$

where η_1 is the transmission efficiency of the grating (which can be specified by the user), $\Xi = (y - \tan(\theta)(x - x_0))/p$, and the symbols $\lfloor \rfloor$ indicate the *floor* operation. In Equation 14, a is a parameter that depends on the type of grating as

$$a = \begin{cases} \eta_2 & \text{for transmission gratings} \\ \eta_2 e^{i\pi/2} & \text{for } \pi/2\text{-shift gratings} \\ \eta_2 e^{i\pi} & \text{for } \pi\text{-shift gratings} \end{cases}. \tag{15}$$

In this case, η_2 corresponds to the transmission efficiency of the phase-shifting part of the grating (for phase gratings) or the attenuating parts (for transmission gratings). Following the definitions above, for a perfect transmission grating $\eta_1 = 1$ and $\eta_2 = 0$, whereas for perfect phase gratings $\eta_1 = \eta_2 = 1$.

Of course, if the user specifies vertical fringes instead, the condition in Equation 14 is modified, inverting the x and y coordinates. As mentioned above, for the first grating, $\theta = 0$.

Finally, denoting the beamsplitter grating as G_1, the wavefront entering the interferometer is calculated as

$$E_{G1}(x,y) = E_{Plasma}(x,y) \cdot G_1(x,y). \tag{16}$$

B. Diffraction solver

Once the wavefront $E_{G1}(x,y)$ has been calculated using Equation 16, the second part of the code calculates the diffraction of this wave when travelling through the interferometer.

The Talbot effect is merely a consequence of the diffraction of a plane wave by a grating[45]. Considering Equation 3, it can be seen that over the lengths involved in Talbot interferometry, since $p \gg \lambda$, the following condition is satisfied:

$$\frac{d_m^3 \lambda}{p^4} = \left(\frac{p}{\lambda}\right)^2 \frac{m^3}{8} \gg 1, \tag{17}$$

which permits treating the problem using the Fresnel diffraction approximation. It is therefore possible to express the free-space propagation of the generated wavefront as

$$E(x,y) = \frac{e^{ikz}}{i\lambda z} \iint_{-\infty}^{+\infty} E_{G1}(x',y') \times e^{\frac{ik}{2z}\left[(x-x')^2+(y-y')^2\right]} dx'dy', \tag{18}$$

where (x',y') are the coordinates of points in the grating, k and λ are the wavenumber and wavelength of the wave, and z is the distance in the propagation direction, measured from the grating.

Solving this equation numerically, although possible, requires an extremely high spatial resolution (to resolve the oscillations of the X-ray wave in a micron-sized field of view), and is computationally expensive. However, that is not necessary, as a significant reduction of the computational cost can be achieved by taking the Fourier transform of Equation 18 and using the so-called *transfer function of the Fresnel diffraction*, H_F. This is expressed as

$$H_F(f_x,f_y,z) = \mathcal{F}\left\{\frac{\exp(ikz)}{i\lambda z}\exp\left[\frac{ik}{2z}\left((x-x')^2+(y-y')^2\right)\right]\right\} = \exp\left\{ikz\left[1-\frac{\lambda^2}{2}\left(f_x^2+f_y^2\right)\right]\right\}, \tag{19}$$

where f_x and f_y are the coordinates in frequency space. It is therefore possible to rewrite Equation 18 as

$$E(x,y) = \mathcal{F}^{-1}\left\{\mathcal{F}(E(x',y',0)) \cdot H_F(f_x,f_y,z)\right\}, \tag{20}$$

thus heavily simplifying the problem[46]. This is the approach that TIA uses to solving the Fresnel diffraction equation.

TIA uses this approach to propagate the wave from the first to the second grating. This process is repeated to apply the second grating's mask and propagate the wavefront to the detector.

Note that TIA does not account for any diffraction effects that occur as the light probes the plasma (as the effects of the plasma are all accounted for using Equation 9), or diffraction from the plasma to the first grating. This approach is valid as long as the angles of diffraction from the plasma itself ($\sim \lambda/L$) fall below the angular resolution of the interferometer[2] ($\sim p_2'/d_m$). This condition can be expressed as

$$\frac{\lambda}{L} \ll \frac{p_2'}{d_m} \rightarrow L \gg p_2'. \tag{21}$$

That is, this approximation is valid when the length scale of the object (usually of the order of tens or hundreds of microns) is larger than the effective period of the second grating after doing the conversion in Equation 7 in the case of Talbot-Lau configuration (usually of the order of microns).

Once the code has calculated the interferometry image generated by the plasma, TIA runs the diffraction solver module a second time, with an unperturbed planar wave (no plasma object) to generate a 'reference' image for comparison.

C. Postprocessing module

The first two modules can be run on their own to produce realistic interferometric images. However, additional postprocessing is required in order to extract the physical properties that can be measured in an actual experiment.

This can be achieved by decomposing the interferometry and reference images in their Fourier components[18,26,47–51] as

$$I(x,y) = I_0(x,y) + \sum_{j=1}^{\infty} I_j(x,y) e^{i\phi_j(x,y)} \approx A(x,y) + B(x,y)e^{i\phi(x,y)}, \tag{22}$$

where $A(x,y)$ corresponds to the attenuated image, $B(x,y)$ is called the *dark field* contribution and $\phi(x,y)$ is the phase shift.

The best approach to obtaining an accurate transmission image is therefore to mask the periodic contributions from the gratings in the Fourier spectrum of the interferometry images. TIA offers two possibilities for the user: automatic peak detection or manual selection. If the former is selected, the code will detect the most intense Fourier peaks up to a certain Fourier order specified by the user. The user can then choose to either mask the regions of the Fourier power spectrum around those peaks that are larger than a certain threshold (also specified by the user), or to mask everything except for a small region around the 0th order. Although this option provides a fast way of postprocessing the interferometry images, in some cases the peak detection algorithm might not detect the correct peaks. In that case, the users might select *Manual selection* and can manually draw rectangles around the regions of the power spectrum that they wish to mask. Supergaussian smoothing is then applied to these rectangular regions in order to avoid hard edges. This allows more freedom to the user but it requires a longer time, as each rectangle needs to be drawn separately.

Once the attenuation mask is designed, an additional mask is required for obtaining the phase image (containing information about B and ϕ). For this purpose, the code offers

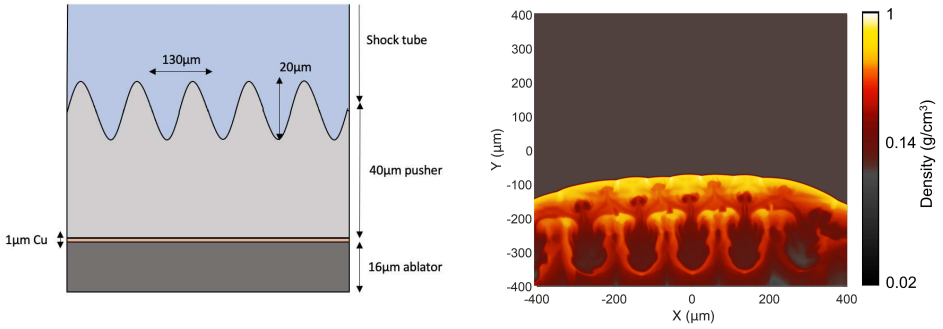

(a) (b)

FIG. 4. (4a) Original target design and (4b) density map at 30 ns for the example simulation. The density figure is presented in logarithmic scale to show the different regions of the expanding plasma.

two additional options to the user: keeping only the Fourier peaks or blocking the 0th order. If the first option is selected, the code will only keep the regions that the user has specified around the Fourier peaks (either with the automatic peak detection or by manually selecting them). On the other hand, if the 0th order block option is selected, the phase mask will keep everything in the Fourier spectrum with frequencies greater than or equal to the first Fourier order. It should be noted here that, if the *manual* mask selection mode is chosen, TIA will consider the first drawn rectangle as being the 0th Fourier order and the second one as corresponding to the 1st order. Although the 0th order block method retains some information from the attenuation image in addition to the diffracted components, it has been included in the code as it is a more robust method in the presence of strong noise in the signal.

After the two masks (attenuation and phase) have been designed, the code calculates the A, B and ϕ components of the image (see Equation 22). While A is directly obtained by taking the inverse Fourier Transform of the power spectrum multiplied by the attenuation mask, the process for obtaining the dark field and phase images is slightly different. As the diffracted term has approximately the form $Be^{i\phi}$, after inverting the masked Fourier transform the code takes the natural logarithm of the generated image and separates the real ($\log(B)$) and imaginary (ϕ) parts. As this last component ϕ is obtained in units of 2π, TIA then proceeds to unwrap the phase following the procedure described by Giglia and Romero[52]; in order to convert it to phase shift units.

Finally, TIA returns three images, corresponding to the so-called attenuation, dark field and phase shifts produced by the plasma object (obj) with respect to the reference image (ref). These are calculated as

$$\text{Attenuation} = \frac{A_{obj}}{A_{ref}}, \tag{23}$$

$$\text{Dark Field} = \frac{B_{obj}}{B_{ref}} \cdot \frac{A_{ref}}{A_{obj}}, \tag{24}$$

$$\phi = \phi_{obj} - \phi_{ref}. \tag{25}$$

It should be noted here that, although these names are commonly found in the literature, they are not exactly accurate. Yang *et al.*[53] showed that both the *attenuation* and *dark field* images contain phase effects from the second-order derivative (the dark field image can even be dominated by these effects), which can enhance edges within the target significantly. However, in this paper we will use the common nomenclature for these images in order to avoid confusion.

IV. EXAMPLE CASE : THE RAYLEIGH-TAYLOR INSTABILITY

To illustrate the full operation of the TIA code, we present here its application to characterize turbulent regimes like those that can be encountered at laser facilities in HED studies[54–56]. We modelled a multilayered target which enables to study the growth of the Rayleigh-Taylor instability[57,58] using a design based on recent experiments by Rigon *et al.*[38,59] in which a laser-generated plasma was decelerated in a low-density foam. To do so, we ran FLASH simulations in which a 2 ns laser square pulse with an intensity of 10^{14} W cm^{-2} and a focal spot 800 µm in diameter irradiates a target such as the one presented in Figure 4a. The laser impinges upon a 16 µm-thick plastic ablator (density 1.044 g cm^{-3}), launching a shock in the target. On top of the ablator there is a 1 µm-thick Cu layer, to prevent pre-heating of the target from the X-ray emission of the coronal plasma generated in the laser-target interface.

The shock is then transferred to a 40 µm-thick plastic pusher (density 1.3 g cm^{-3}) doped with 30% Br. This dopant is used to increase X-ray absorption in the target, and therefore the contrast. To seed the Rayleigh-Taylor instability, a sinusoidal perturbation with 130 µm periodicity and 20 µm peak-to-valley amplitude is imprinted in the rear surface of the pusher along the x direction. Finally, a 1 mm-long shock tube of 0.1 g cm^{-3} carbonized-resorcinol-formaldehyde (CRF) foam, is mounted to observe the instability growth.

The case analyzed here, the density profile of which is shown in Figure 4b, corresponds to the expanding plasma

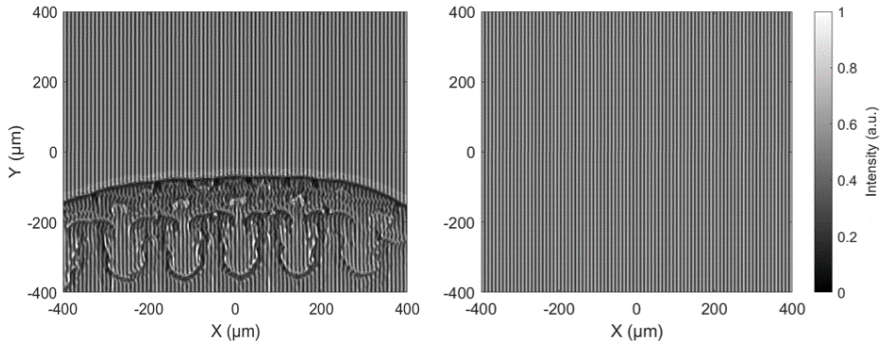

(a) (b)

FIG. 5. Interferometry (5a) and reference (5b) images generated by TIA for the example case shown in Figure 4b.

TABLE I. Values taken for the different parameters of the selected example *experimental* setup.

Parameter	**Value**
Radiation photon energy	7000 eV
Beamsplitter period	5 µm
Beamsplitter fringe orientation	Horizontal
Beamsplitter type	π-shift
Beamsplitter efficiency parameters (η_1, η_2)	0.982, 0.964
Analyzer period	2.5 µm
Analyzer type	Transmission
Analyzer efficiency parameters (η_1, η_2)	0.982, 0.001
Talbot order	3
Distance to detector	5 cm
Angle between gratings	15 °
Detector resolution (on target)	3 µm FWHM
Noise level	10%

at t=30 ns after the start of the laser pulse. The figure is presented in a logarithmic color scale to highlight all the different regions of the plasma.

These experiments were designed to generate a plasma uniform along z, and so the targets are uniform in that direction (the seeded instability seems to be *plowed* along z). Additionally, the laser spots were smoothed to not generate additional imprint instabilities. For this reason, since in our simulation the laser spot is a third-order supergaussian 800 µm in diameter, to avoid effects from the edges of the laser spot, the system was assumed to have a constant thickness of 500 µm in the z-direction. The parameters of the experimental setup chosen in this case are shown in Table I. The distance between gratings is specified as the Talbot order m of the beamsplitter (see Equation 3). The beamsplitter fringes were oriented horizontally, which together with the angle between gratings generates vertically oriented Moiré fringes with a periodicity of ~ 9.5 µm (see Equation 5).

The grating parameters η_1 and η_2 in the example have been chosen to match commercially available gratings. These correspond to MicroWorks GmbH X-ray gratings, which use a polyimide substrate on which, either gold (for transmission gratings) or doped PMMA (π-phase gratings) stripes are grown. From the definitions in Equations 14 and 15, it can be seen that commercially available X-ray diffraction gratings are nearly ideal.

A 3 µm spatial resolution was used in order to be able to resolve the Moiré fringes. This resolution is similar to that in Rigon *et al.*[59], where they obtained a $\sim$ 1 µm resolution by using lithium fluoride (LiF) detectors. Other options that can be used to achieve similar results include high-resolution ceramic X-ray detectors like those at SACLA[60]. Nevertheless, the spatial resolution indicated in Table I corresponds to *on target* resolution, so if TIA is used in Talbot-Lau mode, magnification must be taken into account. For example, if an object magnification ~ 40 is used[11], a resolution of 3 µm can be easily obtained using regular CCD cameras.

The synthetic interferometry images generated, object and reference, are shown in Figure 5. In the first image it can be seen how the light is deflected and absorbed by the plasma, imprinting a pattern on the fringes that can be analyzed when compared to the reference image. These differences are sufficient to retrieve important information about the plasma after the TIA postprocessing module is executed.

For this example, the 'Manual' mode of the postprocessing module was chosen, selecting the areas around the first and second Fourier orders and a *'Fourier peaks'* phase mask was used. Recall that this means that the manually-selected regions around the first and second order Fourier peaks were masked in order to obtain an attenuation image, while they were the only components kept for the phase images.

The results are shown in Figure 6, where 6a corresponds to the attenuation image, 6b to the dark field and 6c to the phase shift. The contrast of each image has been adjusted to ease the visualization of the different features of the plasma. Additionally, Figure 6d shows 20 µm-wide horizontal lineouts through $y = -360$ µm as indicated by the dashed horizontal lines, together with the equivalent density lineout from the

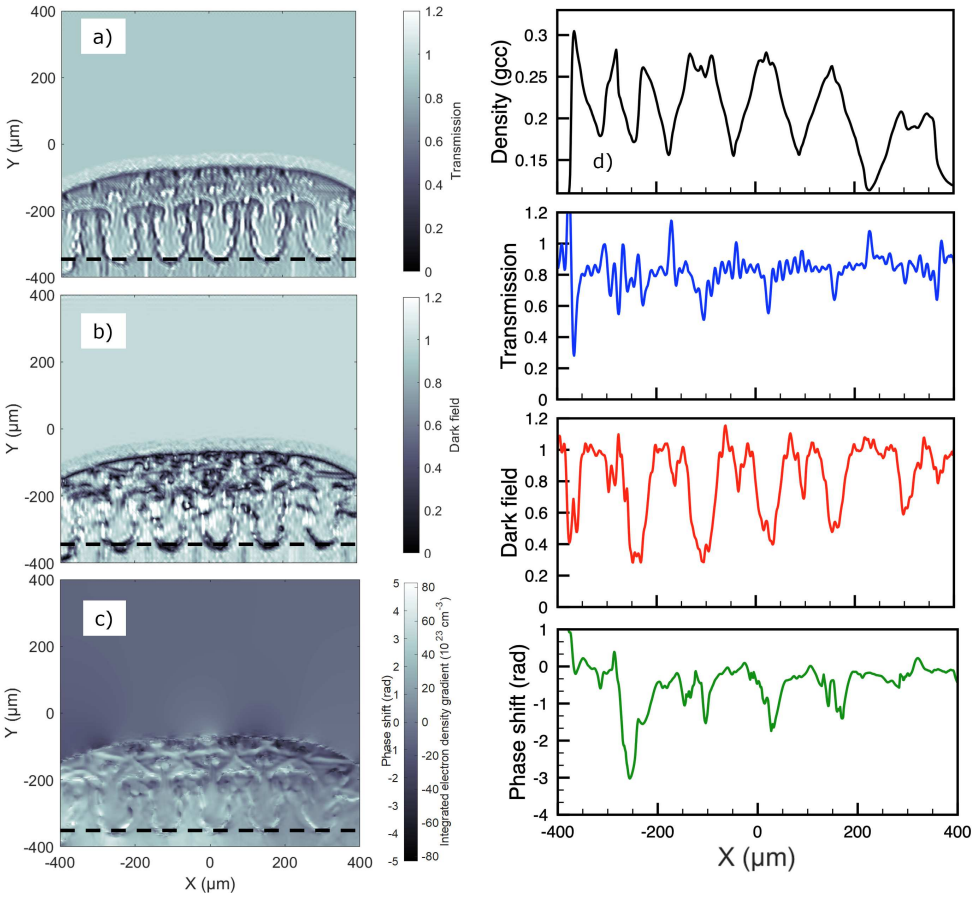

FIG. 6. Results from the example case. (a) Transmission image, (b) dark field image and (c) phase shift. The colorbars and contrast have been adjusted so that the features of the plasma can be easily observed in all images. An additional scale has been added to the phase shift figure, indicating the equivalent values of the integrated electron density gradient $\left(\vec{\nabla}\left(n_e z\right)\right)$ that can be measured with this system. Panel (d) shows 20 µm-wide horizontal lineouts through $y = -360\,\mu$m together with the corresponding density lineout from the hydrodynamic simulation in Figure 4b for comparison. This position is indicated by the horizontal dashed lines in (a)-(c). Note how the transmission contrast in this case is very low compared with the dark field features, illustrating the advantages of Talbot interferometry over absorption radiography in such regimes.

hydrodynamic simulation (Figure 4b) for the sake of comparison.

The measured transmission reaches values slightly above one at some points in the plasma. This is an indication of the second-order derivative effects that were mentioned in the previous section, which arise from the presence of strong density gradients in a direction perpendicular to the wave propagation, such as sharp edges in the object. This effect is commonly known as *refraction enhancement*[61,62] and is of particular interest for the dense plasma community for characterizing irregularities in the surface of targets, such as ICF capsules[63–65].

It can be seen that the periodic features of the instability are obtained with a much larger contrast in the dark field image than in the transmission image. This is due to the very strong density gradients in those regions.

Additionally, the colorbar in Figure 6c shows how the phase shift image can be easily converted to units of electron density

gradient by applying the following transformation[12]

$$\vec{\nabla}\left(n_e z\right) = \frac{\phi}{\lambda^2 r_e} \cdot \frac{p_2'}{d_m}, \tag{26}$$

where λ is the wavelength of the X-rays, r_e is the classical electron radius, z is the thickness of the plasma object (500 µm in this particular example), p_2' is the period of the analyzer grating (transformed in the case of Talbot-Lau operation) and d_m is the distance between the beamsplitter and the analyzer.

V. CONCLUSIONS

We have presented TIA, a software tool that can simulate a complete experimental setup with a Talbot or a Talbot-Lau interferometer using the output of 2D FLASH hydrodynamic simulations as input. This code can be used as a testbed for experimental designs which include X-ray interferometry to accurately predict obtainable measurements and help decide on the experimental parameters.

In order to achieve this, TIA has three different modules: wavefront calculator, diffraction solver, and postprocessing module. The first calculates the changes in the wavefront introduced by the plasma of consideration (both phase shifts and absorption). After that, the diffraction solver calculates the Fresnel diffraction pattern of the generated wavefront as it traverses the interferometer to the detector. Finally, the postprocessing module can be used to extract the absorption, dark field and phase shift components of the generated interferometry images.

We have presented an example of the operation of TIA, probing a laser-generated Rayleigh-Taylor instability using a 7 keV radiation source. We have shown how, even small features in the interference pattern can translate into significant features in the phase images, which present more detail than the classical absorption image used in X-ray radiography. Future work includes testing the output from this code against laser-plasma experimental data obtained at XFEL facilities such as SACLA[29,59] and the European XFEL.

ACKNOWLEDGEMENTS

The FLASH software was developed in part by the DOE NNSA ASC- and DOE Office of Science ASCR-supported Flash Center for Computational Science at the University of Chicago. We acknowledge support from the France And Chicago Collaborating in The Sciences (FACCTS) Program.

This work has been funded by the National Nuclear Security Administration (DENA0003882), the Conseil Règional Aquitaine (INTALAX) and the Agence Nationale de la Recherche (ANR-10-IDEX-03-02, ANR-15-CE30-0011). G.P.-C. acknowledges support from the Spanish Ministry of Science and Innovation through the *Margarita Salas* funding program.

Data availability: Simulations underlying the results presented in this paper may be obtained from the authors upon reasonable request. The TIA code has been packaged into a standalone application using the Matlab App Designer module, and is available upon request to the authors.

Conflicts of interest: The authors declare no conflicts of interest.

[1] J. Kilkenny, G. Richau, C. Sangster, S. Batha, P. Bell, D. Larson, D. Bradley, R. Leeper, H. Herrmann, C. Bourdon, *et al.*, "The icf national diagnostic plan (ndp) 9/19/17," Tech. Rep. (Lawrence Livermore National Lab.(LLNL), Livermore, CA (United States), 2017).

[2] D. Stutman and M. Finkenthal, "Talbot-Lau x-ray interferometry for high energy density plasma diagnostic," Review of Scientific Instruments **82**, 113508 (2011).

[3] H. F. Talbot, "LXXVI. Facts relating to optical science. No. IV," The London, Edinburgh, and Dublin Philosophical Magazine and Journal of Science **9**, 401–407 (1836).

[4] E. Lau, "Beugungserscheinungen an doppelrastern," Annalen der Physik **437**, 417–423 (1948).

[5] J. Kiyohara, C. Makifuchi, K. Kido, S. Nagatsuka, J. Tanaka, M. Nagashima, T. Endo, S. Ichihara, W. Yashiro, and A. Momose, "Development of the talbot-lau interferometry system available for clinical use," (American Institute of Physics, 2012) pp. 97–102.

[6] F. Horn, M. Leghissa, S. Kaeppler, G. Pelzer, J. Rieger, M. Seifert, J. Wandner, T. Weber, T. Michel, C. Riess, and G. Anton, "Implementation of a talbot-lau interferometer in a clinical-like c-arm setup: A feasibility study," Scientific reports **8**, 1–11 (2018).

[7] J. Nejdl, M. Kozlová, T. Mocek, and B. Rus, "Measuring the electron density gradients of dense plasmas by deflectometry using short-wavelength probe," Physics of Plasmas **17**, 122705 (2010).

[8] M. Valdivia, D. Stutman, and M. Finkenthal, "Talbot-Lau based Moiré deflectometry with non-coherent sources as potential High Energy Density plasma diagnostic," Journal of Applied Physics **114**, 163302 (2013).

[9] M. Valdivia, D. Stutman, and M. Finkenthal, "Moire deflectometry using the Talbot-Lau interferometer as refraction diagnostic for high energy density plasmas at energies below 10 keV," Review of Scientific Instruments **85**, 073702 (2014).

[10] M. Valdivia, D. Stutman, and M. Finkenthal, "Single-shot z eff dense plasma diagnostic through simultaneous refraction and attenuation measurements with a talbot–lau x-ray moiré deflectometer," Applied optics **54**, 2577–2583 (2015).

[11] M. Valdivia, D. Stutman, C. Stoeckl, C. Mileham, J. Zou, S. Muller, K. Kaiser, C. Sorce, P. Keiter, J. Fein, M. Trantham, R. P. Drake, and S. P. Regan, "Implementation of a Talbot-Lau x-ray deflectometer diagnostic platform for the OMEGA EP laser," Review of Scientific Instruments **91**, 023511 (2020).

[12] M. P. Valdivia, F. Veloso, D. Stutman, C. Stoeckl, C. Mileham, I. A. Begishev, W. Theobald, M. Vescovi, W. Useche, S. P. Regan, B. Albertazzi, G. Rigon, P. Mabey, T. Michel, S. A. Pikuz, M. Koenig, and A. Casner, "X-ray backlighter requirements for refraction-based electron density diagnostics through talbot-lau deflectometry," Review of Scientific Instruments **89**, 10G127 (2018).

[13] G.P.-C. wishes to mention that the name of the TIA code is intended as an homage to the work of Francisco Ibáñez.

[14] A. Momose, S. Kawamoto, I. Koyama, Y. Hamaishi, K. Takai, and Y. Suzuki, "Demonstration of x-ray talbot interferometry," Japanese journal of applied physics **42**, L866 (2003).

[15] T. Weitkamp, A. Diaz, C. David, F. Pfeiffer, M. Stampanoni, P. Cloetens, and E. Ziegler, "X-ray phase imaging with a grating interferometer," Optics express **13**, 6296–6304 (2005).

[16] T. Weitkamp, C. David, C. Kottler, O. Bunk, and F. Pfeiffer, "Tomography with grating interferometers at low-brilliance sources," in *Developments in X-Ray Tomography V*, Vol. 6318 (International Society for Optics and Photonics, 2006) p. 63180S.

[17] F. Pfeiffer, T. Weitkamp, O. Bunk, and C. David, "Phase retrieval and differential phase-contrast imaging with low-brilliance x-ray sources," Nature physics **2**, 258–261 (2006).

[18] F. Pfeiffer, M. Bech, O. Bunk, P. Kraft, E. F. Eikenberry, C. Brönnimann, C. Grünzweig, and C. David, "Hard-x-ray dark-field imaging using a grating interferometer," Nature materials **7**, 134–137 (2008).

[19] J. Krasinski, D. F. Heller, and O. Kafri, "Phase object mi-

croscopy using moire deflectometry," Applied optics **24**, 3032–3036 (1985).
[20]B. Moosman, V. Bystritskii, C. Boswell, and F. Wessel, "Moire deflectometry diagnostic for transient plasma, using a multipulse n2 laser," Review of scientific instruments **67**, 170–177 (1996).
[21]J. Ruiz-Camacho, F. Beg, and P. Lee, "Comparison of sensitivities of moire deflectometry and interferometry to measure electron densities in z-pinch plasmas," Journal of Physics D: Applied Physics **40**, 2026 (2007).
[22]J. Valenzuela, E. Wyndham, H. Chuaqui, D. Cortes, M. Favre, and H. Bhuyan, "Implementation of moiré-schlieren deflectometry on a small scale fast capillary plasma discharge," Journal of Applied Physics **111**, 103301 (2012).
[23]D. Stutman, M. P. Valdivia, and M. Finkenthal, "X-ray Moiré deflectometry using synthetic reference images," Applied optics **54**, 5956–5961 (2015).
[24]J. Valenzuela, E. Wyndham, and M. Favre, "Time-resolved study of the extreme-ultraviolet emission and plasma dynamics of a sub-joule, fast capillary discharge," Physics of Plasmas **22**, 083501 (2015).
[25]S. Bachche, M. Nonoguchi, K. Kato, M. Kageyama, T. Koike, M. Kuribayashi, and A. Momose, "Laboratory-based x-ray phase-imaging scanner using talbot-lau interferometer for non-destructive testing," Scientific reports **7**, 1–7 (2017).
[26]M. Seifert, M. Gallersdörfer, V. Ludwig, M. Schuster, F. Horn, G. Pelzer, J. Rieger, T. Michel, and G. Anton, "Improved reconstruction technique for moire imaging using an x-ray phase-contrast talbot–lau interferometer," Journal of Imaging **4**, 62 (2018).
[27]S. Balovsiak, S. Novikov, I. Fodchuk, and I. Yaremchuk, "Analysis of moiré x-ray images of deformed crystals using radial distribution of the fourier energy spectrum," Metallophysics and Advanced Technologies **41**, 389–402 (2019).
[28]H. Lee, D. Jeon, H. Lim, H. Cho, M. Park, and W. Youn, "Quantification of the effects of grid angulation on image quality in single-grid-based phase-contrast x-ray imaging," Journal of Optics (2021).
[29]T. Tschentscher, M. Altarelli, R. Brinkmann, T. Delissen, A. Schwarz, and K. Witte, "Technical Report: The European X-ray Free-Electron Laser Facility: A New Infrastructure for Research Using Ultrashort, Coherent X-ray Pulses of Extreme Brightness," Synchrotron Radiation News **19**, 13–19 (2006).
[30]G. Geloni, E. Saldin, L. Samoylova, E. Schneidmiller, H. Sinn, T. Tschentscher, and M. Yurkov, "Coherence properties of the European XFEL," New Journal of Physics **12**, 035021 (2010).
[31]D. Pile, "First light from SACLA," Nature Photonics **5**, 456–457 (2011).
[32]J. Arthur, G. Materlik, R. Tatchyn, and H. Winick, "The LCLS: A fourth generation light source using the SLAC linac," Review of scientific instruments **66**, 1987–1989 (1995).
[33]E. Saldin, E. Schneidmiller, and M. Yurkov, "Coherence properties of the radiation from sase fel," Nuclear Instruments and Methods in Physics Research Section A: Accelerators, Spectrometers, Detectors and Associated Equipment **507**, 106–109 (2003).
[34]J. Jahns and A. W. Lohmann, "The Lau effect (a diffraction experiment with incoherent illumination)," Optics communications **28**, 263–267 (1979).
[35]B. Fryxell, K. Olson, P. Ricker, F. Timmes, M. Zingale, D. Lamb, P. MacNeice, R. Rosner, J. Truran, and H. Tufo, "Flash: An adaptive mesh hydrodynamics code for modeling astrophysical thermonuclear flashes," The Astrophysical Journal Supplement Series **131**, 273 (2000).
[36]A. Dubey, K. Antypas, M. K. Ganapathy, L. B. Reid, K. Riley, D. Sheeler, A. Siegel, and K. Weide, "Extensible component-based architecture for flash, a massively parallel, multiphysics simulation code," Parallel Computing **35**, 512–522 (2009).
[37]P. Tzeferacos, M. Fatenejad, N. Flocke, C. Graziani, G. Gregori, D. Lamb, D. Lee, J. Meinecke, A. Scopatz, and K. Weide, "Flash mhd simulations of experiments that study shock-generated magnetic fields," High Energy Density Physics **17**, 24–31 (2015).
[38]G. Rigon, A. Casner, B. Albertazzi, T. Michel, P. Mabey, E. Falize, J. Ballet, L. Van Box Som, S. Pikuz, Y. Sakawa, T. Sano, A. Faenov, T. Pikuz, N. Ozaki, Y. Kuramitsu, M. P. Valdivia, P. Tzeferacos, D. Lamb, and M. Koenig, "Rayleigh-Taylor instability experiments on the LULI2000 laser in scaled conditions for young supernova remnants," Phys. Rev. E **100**, 021201 (2019).
[39]P. Tzeferacos, A. Rigby, A. F. A. Bott, A. R. Bell, R. Bingham, A. Casner, F. Cattaneo, E. M. Churazov, J. Emig, F. Fiuza, C. B. Forest, J. Foster, C. Graziani, J. Katz, M. Koenig, C.-K. Li, J. Meinecke, R. Petrasso, H.-S. Park, B. A. Remington, J. S. Ross, D. Ryu, D. Ryutov, T. G. White, B. Reville, F. Miniati, A. A. Schekochihin, D. Q. Lamb, D. H. Froula, and G. Gregori, "Laboratory evidence of dynamo amplification of magnetic fields in a turbulent plasma," Nature Communications **9**, 591 (2018).
[40]J. Nilsen and J. H. Scofield, "Plasmas with an index of refraction greater than 1," Optics letters **29**, 2677–2679 (2004).
[41]F. F. Chen, "Introduction to plasma physics and controlled fusion," (2016).
[42]A. S. Richardson, *2019 NRL plasma formulary* (Naval Research Laboratory, 2019).
[43]G. Williams, H.-K. Chung, S. Vinko, S. Künzel, A. Sardinha, P. Zeitoun, and M. Fajardo, "Method of time resolved refractive index measurements of x-ray laser heated solids," Physics of Plasmas **20**, 042701 (2013).
[44]K. Wieseman, "A short introduction to plasma physics," CAS-CERN Accelerator School: Ion Sources (2014).
[45]L. Rayleigh, "XXV. On copying diffraction-gratings, and on some phenomena connected therewith," The London, Edinburgh, and Dublin Philosophical Magazine and Journal of Science **11**, 196–205 (1881).
[46]J. Li, Z. Peng, and Y. Fu, "Diffraction transfer function and its calculation of classic diffraction formula," Optics Communications **280**, 243–248 (2007).
[47]M. Engelhardt, C. Kottler, O. Bunk, C. David, C. Schroer, J. Baumann, M. Schuster, and F. Pfeiffer, "The fractional talbot effect in differential x-ray phase-contrast imaging for extended and polychromatic x-ray sources," Journal of Microscopy **232**, 145–157 (2008).
[48]N. Bevins, J. Zambelli, K. Li, Z. Qi, and G.-H. Chen, "Multicontrast x-ray computed tomography imaging using talbot-lau interferometry without phase stepping," Medical physics **39**, 424–428 (2012).
[49]A. Malecki, G. Potdevin, and F. Pfeiffer, "Quantitative wave-optical numerical analysis of the dark-field signal in grating-based x-ray interferometry," EPL (Europhysics Letters) **99**, 48001 (2012).
[50]S. Gkoumas, P. Villanueva-Perez, Z. Wang, L. Romano, M. Abis, and M. Stampanoni, "A generalized quantitative interpretation of dark-field contrast for highly concentrated microsphere suspensions," Scientific reports **6**, 1–8 (2016).
[51]V. Bouffetier, L. Ceurvorst, M. Valdivia, F. Dorchies, S. Hulin, T. Goudal, D. Stutman, and A. Casner, "Proof-of-concept Talbot-Lau x-ray interferometry with a high-intensity, high-repetition-rate, laser-driven K-alpha source," Applied optics **59**, 8380–8387 (2020).
[52]D. C. Ghiglia and L. A. Romero, "Robust two-dimensional weighted and unweighted phase unwrapping that uses fast transforms and iterative methods," JOSA A **11**, 107–117 (1994).
[53]Y. Yang and X. Tang, "The second-order differential phase contrast and its retrieval for imaging with x-ray talbot interferometry," Medical physics **39**, 7237–7253 (2012).
[54]C. C. Kuranz, H.-S. Park, C. M. Huntington, A. R. Miles, B. A. Remington, T. Plewa, M. Trantham, H. Robey, D. Shvarts, A. Shimony, *et al.*, "How high energy fluxes may affect rayleigh–taylor instability growth in young supernova remnants," Nature communications **9**, 1–6 (2018).
[55]A. Casner, "Recent progress in quantifying hydrodynamics instabilities and turbulence in inertial confinement fusion and high-energy-density experiments," Philosophical Transactions of the Royal Society A **379**, 20200021 (2021).

[56] A. Do, A. Angulo, G. Hall, S. Nagel, N. Izumi, B. Kozioziemski, T. McCarville, J. Ayers, and D. Bradley, "X-ray imaging of rayleigh–taylor instabilities using fresnel zone plate at the national ignition facility," Review of Scientific Instruments **92**, 053511 (2021).
[57] A. Casner, C. Mailliet, G. Rigon, S. Khan, D. Martinez, B. Albertazzi, T. Michel, T. Sano, Y. Sakawa, P. Tzeferacos, *et al.*, "From icf to laboratory astrophysics: ablative and classical rayleigh–taylor instability experiments in turbulent-like regimes," Nuclear Fusion **59**, 032002 (2018).
[58] G. Malamud, L. Elgin, T. Handy, C. Huntington, R. Drake, D. Shvarts, A. Shimony, and C. Kuranz, "Design of a single-mode rayleigh–taylor instability experiment in the highly nonlinear regime," High Energy Density Physics **32**, 18–30 (2019).
[59] G. Rigon, B. Albertazzi, T. Pikuz, P. Mabey, V. Bouffetier, N. Ozaki, T. Vinci, F. Barbato, E. Falize, Y. Inubushi, *et al.*, "Micron-scale phenomena observed in a turbulent laser-produced plasma," Nature communications **12**, 1–9 (2021).
[60] T. Kameshima, A. Takeuchi, K. Uesugi, T. Kudo, Y. Kohmura, K. Tamasaku, K. Muramatsu, T. Yanagitani, M. Yabashi, and T. Hatsui, "Development of an x-ray imaging detector to resolve 200 nm line-and-space patterns by using transparent ceramics layers bonded by solid-state diffusion," Optics letters **44**, 1403–1406 (2019).
[61] Y. Ping, O. Landen, D. Hicks, J. Koch, R. Wallace, C. Sorce, B. Hammel, and G. Collins, "Refraction-enhanced x-ray radiography for density profile measurements at ch/be interface," Journal of Instrumentation **6**, P09004 (2011).
[62] J. A. Koch, O. L. Landen, L. J. Suter, and L. P. Masse, "Simple solution to the fresnel–kirchoff diffraction integral for application to refraction-enhanced radiography," J. Opt. Soc. Am. A **30**, 1460–1463 (2013).
[63] B. Kozioziemski, J. Koch, A. Barty, H. Martz Jr, W.-K. Lee, and K. Fezzaa, "Quantitative characterization of inertial confinement fusion capsules using phase contrast enhanced x-ray imaging," Journal of applied physics **97**, 063103 (2005).
[64] J. A. Koch, O. L. Landen, B. J. Kozioziemski, N. Izumi, E. L. Dewald, J. D. Salmonson, and B. A. Hammel, "Refraction-enhanced x-ray radiography for inertial confinement fusion and laser-produced plasma applications," Journal of Applied Physics **105**, 113112 (2009).
[65] J. A. Koch, O. L. Landen, L. J. Suter, L. P. Masse, D. S. Clark, J. S. Ross, A. J. Mackinnon, N. B. Meezan, C. A. Thomas, and Y. Ping, "Refraction-enhanced backlit imaging of axially symmetric inertial confinement fusion plasmas," Applied optics **52**, 3538–3556 (2013).

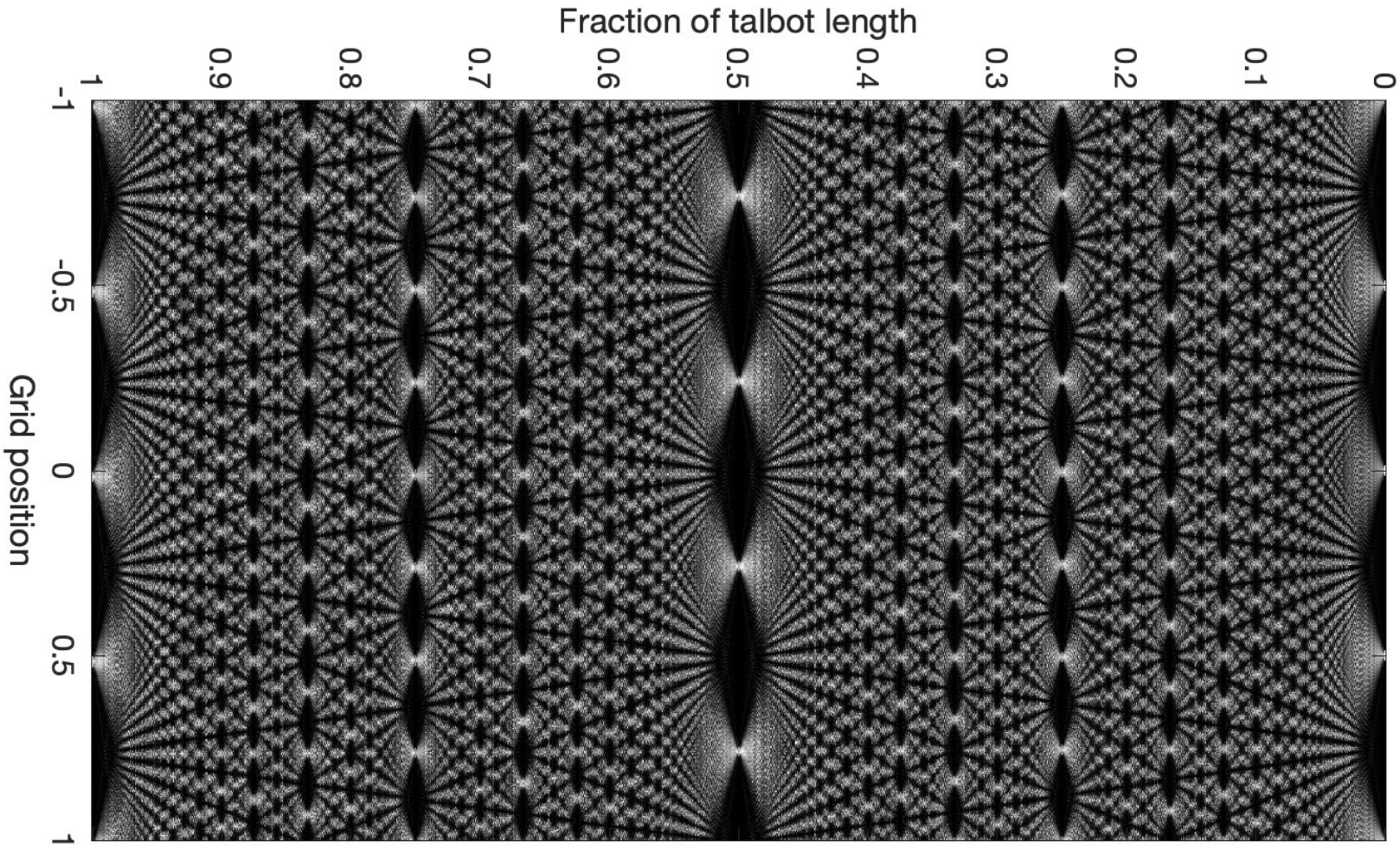

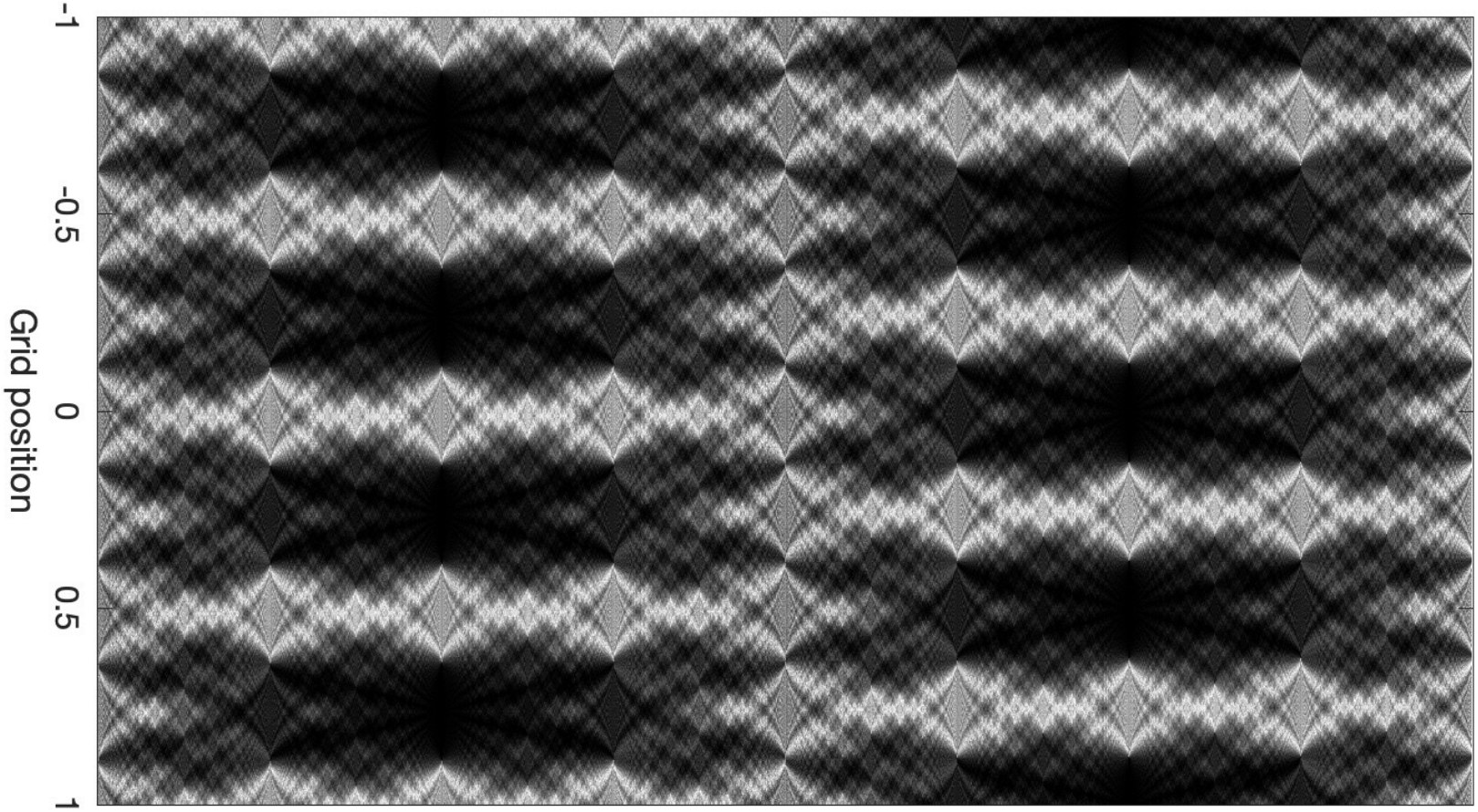

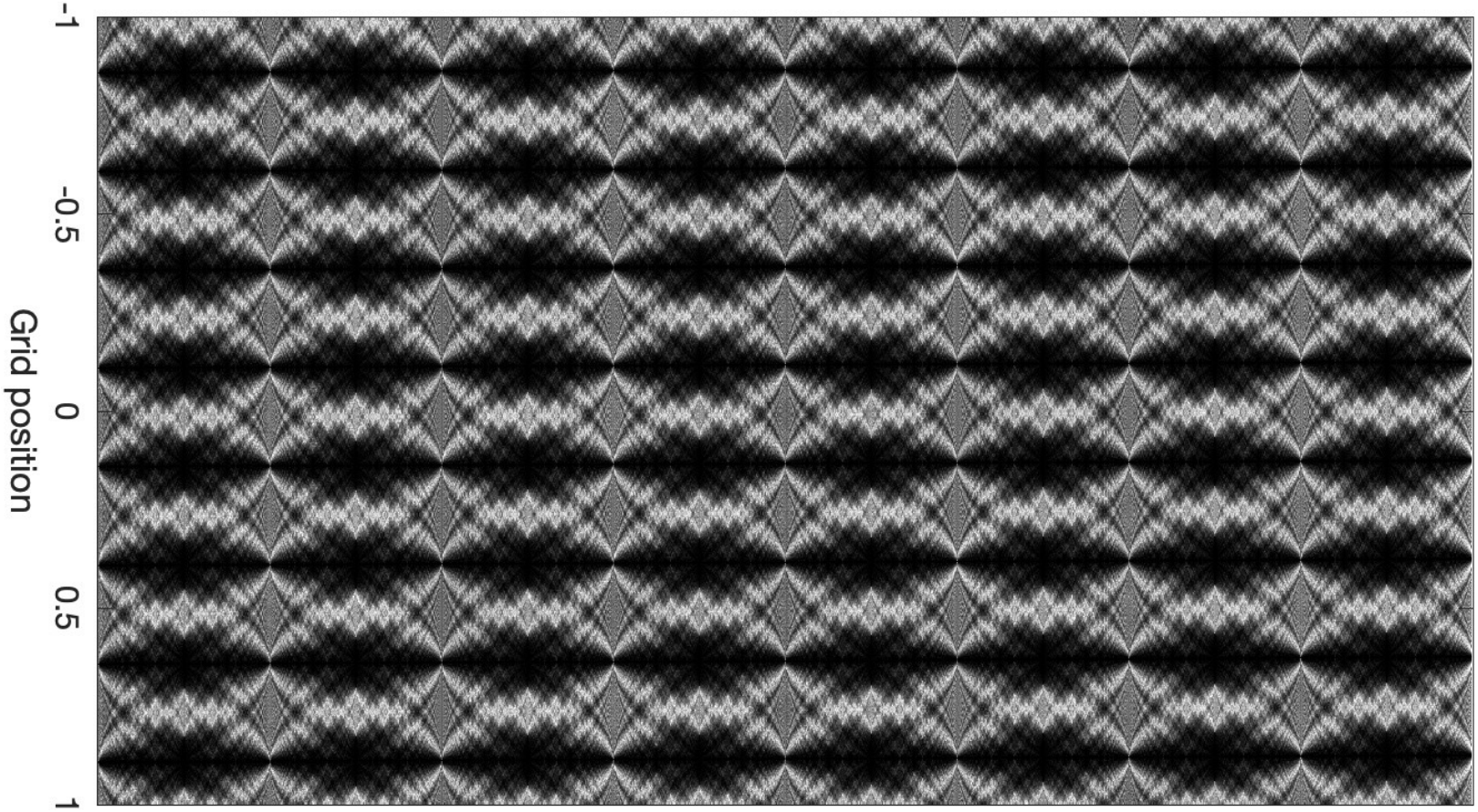

PLEASE CITE THIS ARTICLE AS DOI: 10.1063/5.0085822

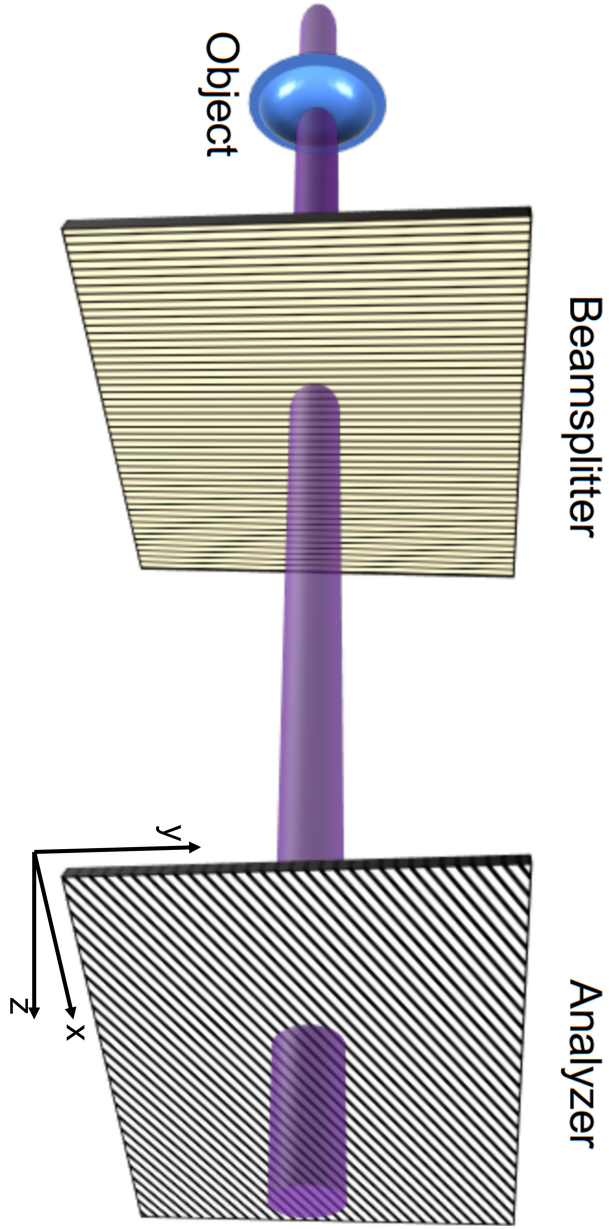

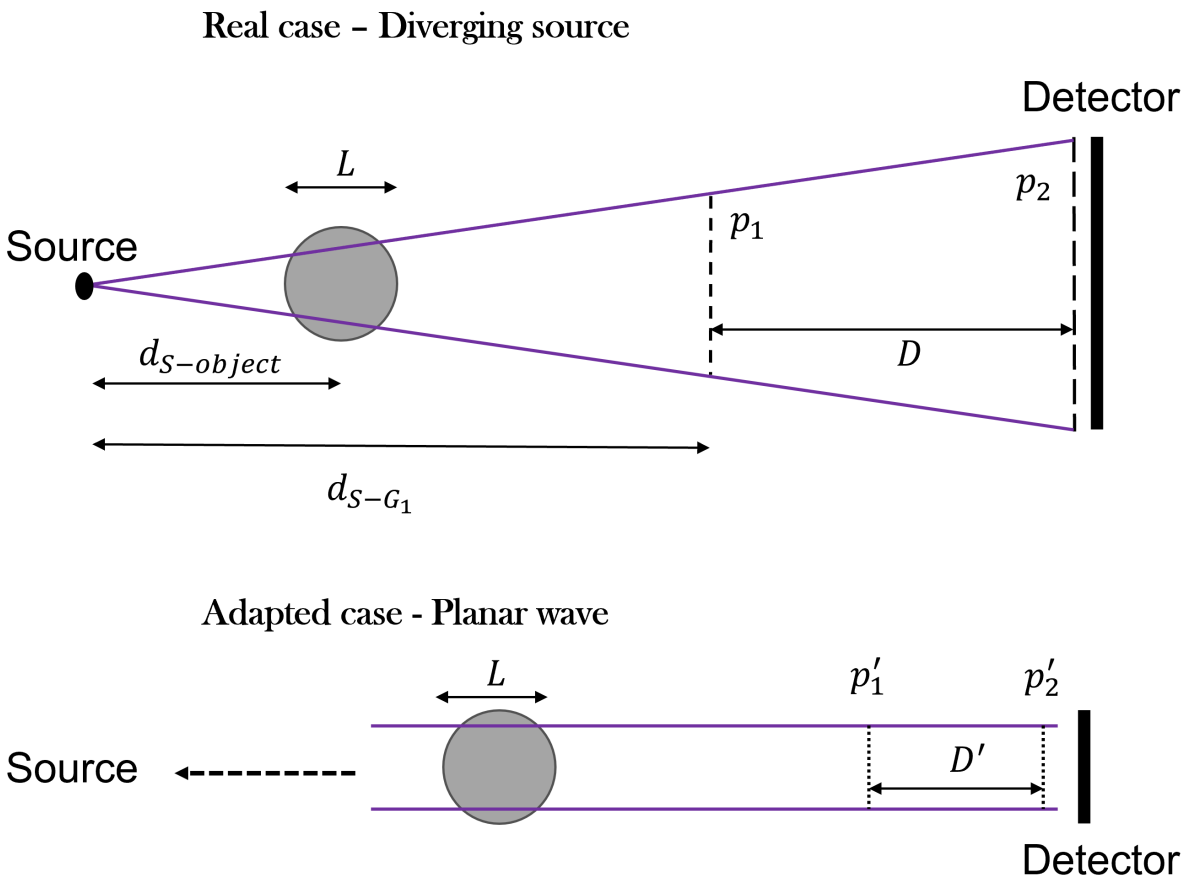

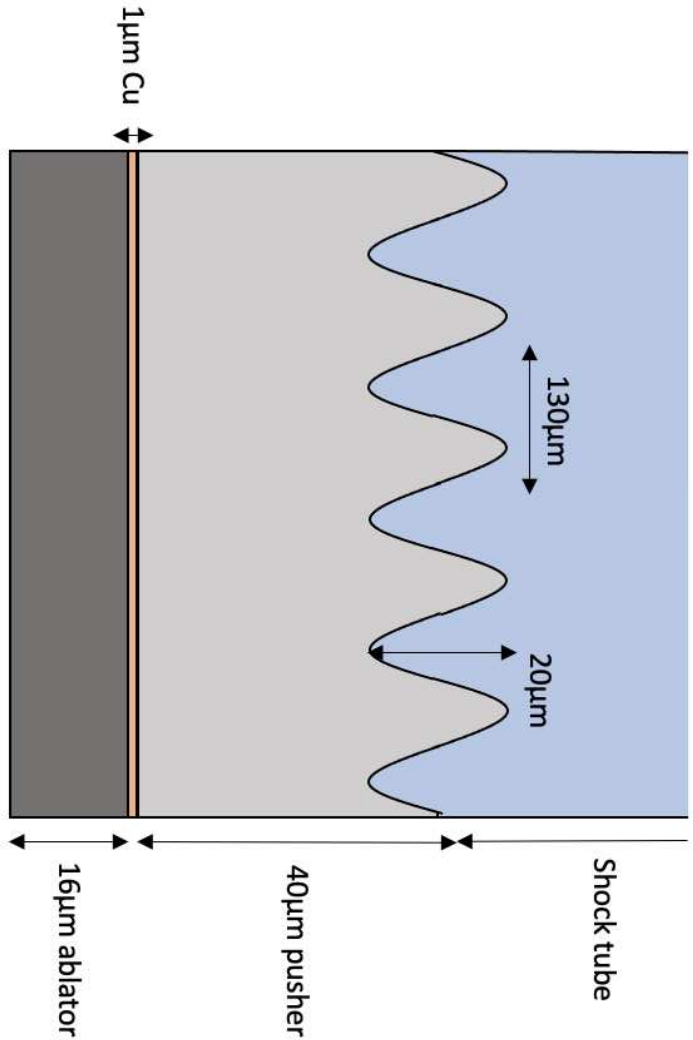

PLEASE CITE THIS ARTICLE AS DOI: 10.1063/5.0085822

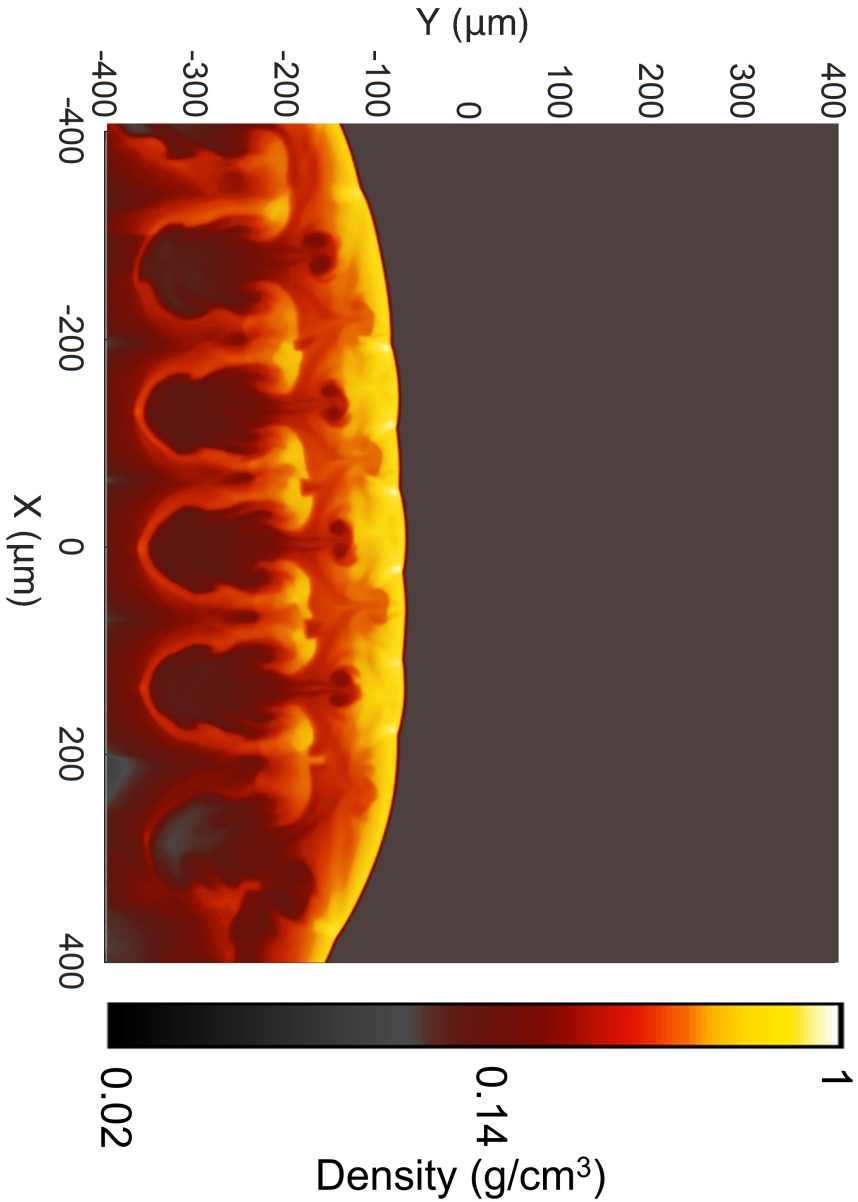

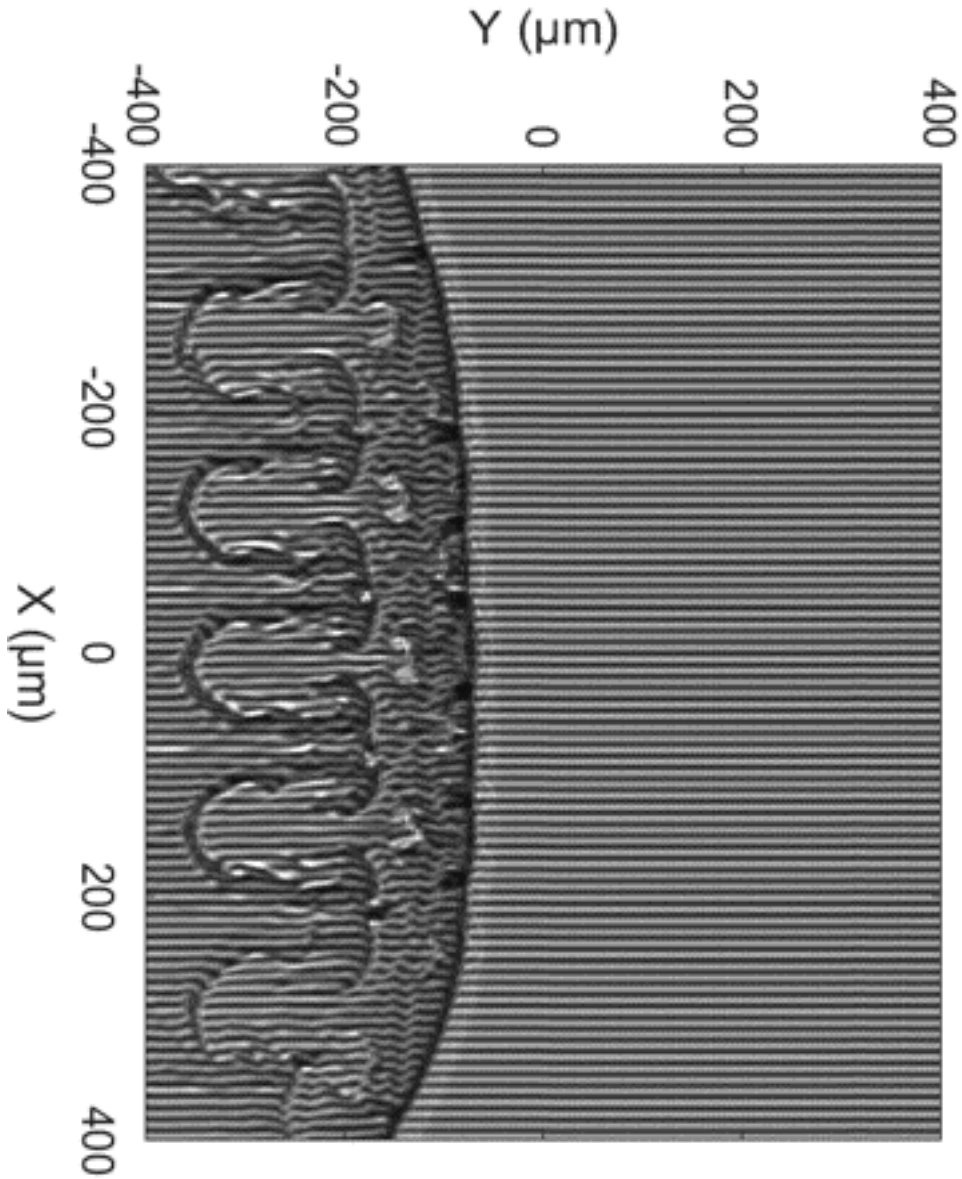

PLEASE CITE THIS ARTICLE AS DOI: 10.1063/5.0085822

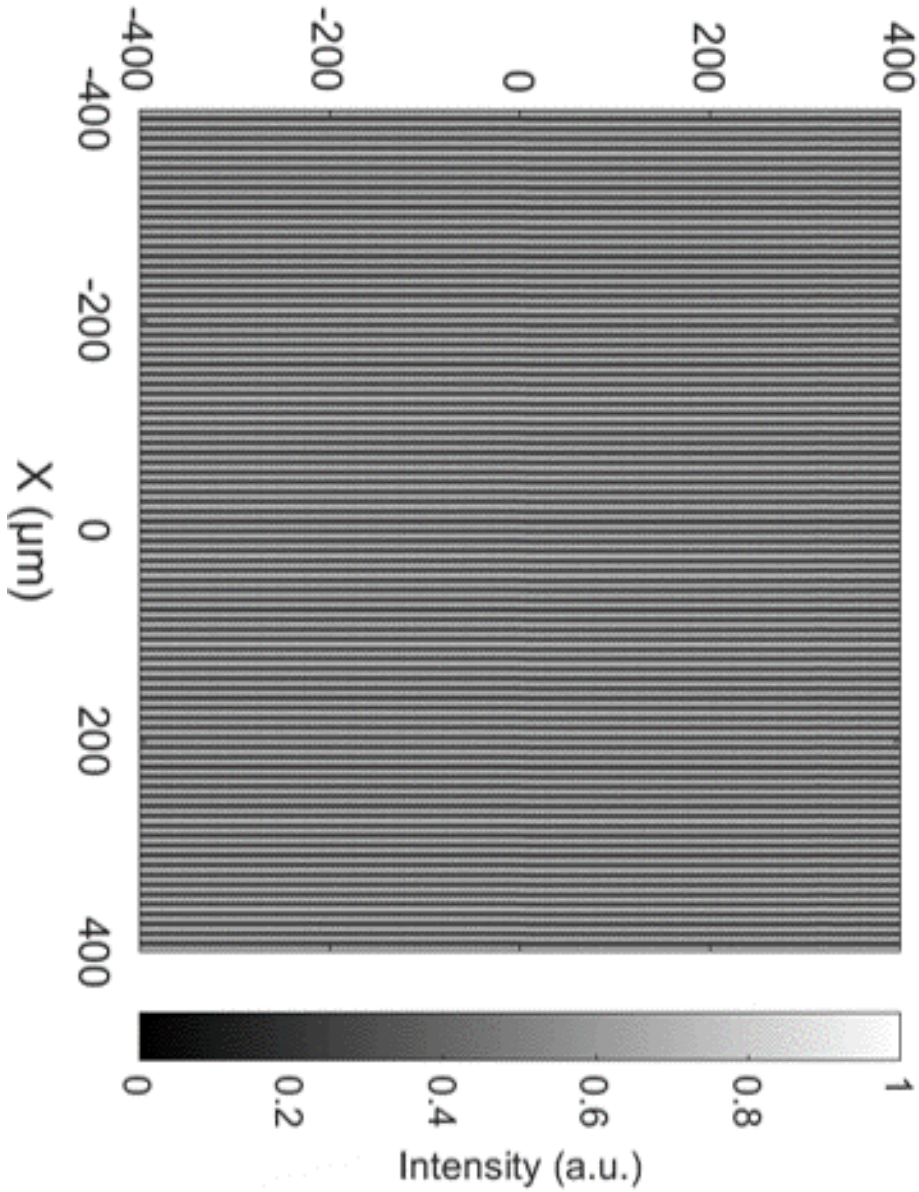

PLEASE CITE THIS ARTICLE AS DOI: 10.1063/5.0085822